Realization of vertical metal/semiconductor heterostructures via solution-phase epitaxy

Wang *et al.*

Supplementary Information

Realization of vertical metal/semiconductor heterostructures via solution-phase epitaxy

Xiaoshan Wang[‡1], Zhiwei Wang[‡1], Jindong Zhang[1], Xiang Wang[1], Zhipeng Zhang[1], Jialiang Wang[1], Zhaohua Zhu[1], Zhuoyao Li[1], Yao Liu[1], Xuefeng Hu[2], Junwen Qiu[2], Guohua Hu[3], Bo Chen[4], Ning Wang[1,4], Qiyuan He[4], Junze Chen[4], Jiaxu Yan[1], Wei Zhang[2], Tawfique Hasan[3], Shaozhou Li[5], Hai Li[1], Hua Zhang[4], Qiang Wang[6]*, Xiao Huang[1]*, Wei Huang[1,5,7]*

1. Institute of Advanced Materials (IAM), Nanjing Tech University (NanjingTech), 30 South Puzhu Road, Nanjing 211816, P. R. China

2. State Key Laboratory of Materials-Oriented Chemical Engineering, College of Chemical Engineering, Nanjing Tech University (NanjingTech), 30 South Puzhu Road, Nanjing 211816, P. R. China

3. Cambridge Graphene Centre, University of Cambridge, Cambridge CB3 0FA, UK

4. Center for Programmable Materials, School of Materials Science and Engineering, Nanyang Technological University, 50 Nanyang Avenue, Singapore 639798, Singapore

5. Key Laboratory for Organic Electronics and Information Displays & Institute of Advanced Materials, Jiangsu National Synergistic Innovation Center for Advanced Materials (SICAM), Nanjing University of Posts & Telecommunications, 9 Wenyuan Road, Nanjing 210023, P. R. China

6. School of Chemistry and Molecular Engineering, Nanjing Tech University (NanjingTech), 30 South Puzhu Road, Nanjing 211816, P. R. China

7. Shaanxi Institute of Flexible Electronics (SIFE), Northwestern Polytechnical University (NPU), 127 West Youyi Road, Xi'an 710072, P. R. China

Supplementary Figures

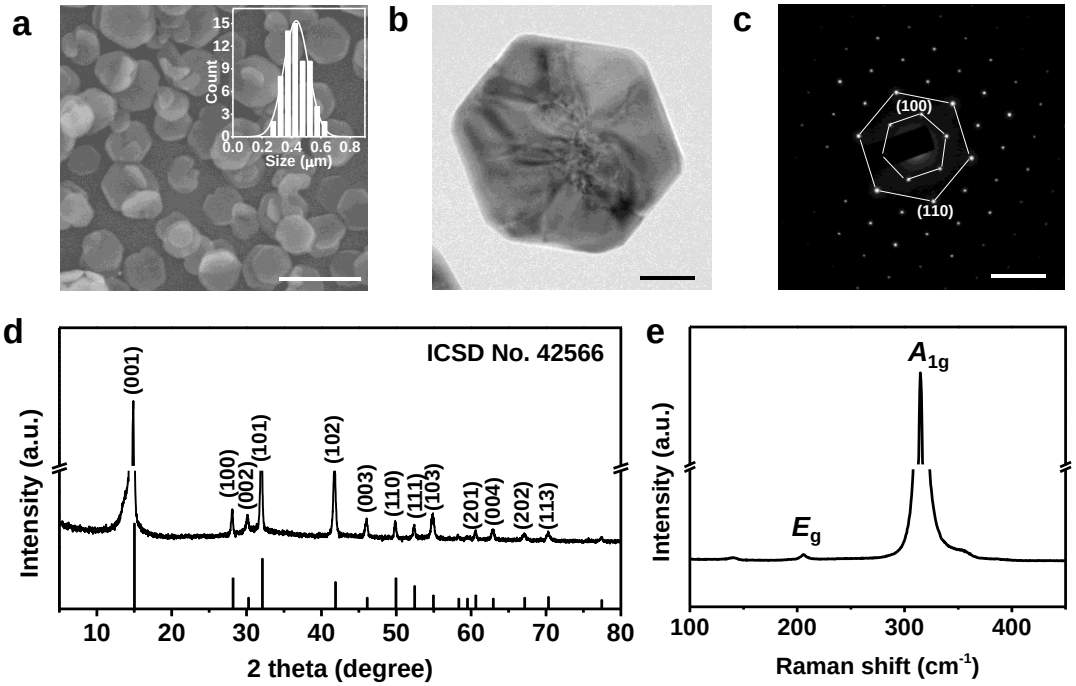

Supplementary Figure 1. (a) SEM image (scale bar, 500 nm), (b) TEM image (scale bar, 100 nm), (c) SAED pattern (scale bar, 5 nm^{-1}), (d) XRD pattern and (e) Raman spectrum of SnS_2 nanoplates. Inset of (a): lateral size distribution of the nanoplates. Raman spectrum in (e) shows two dominant peaks at 205 and 314 cm^{-1} corresponding to the E_g and A_{1g} vibrational modes of SnS_2, respectively[1].

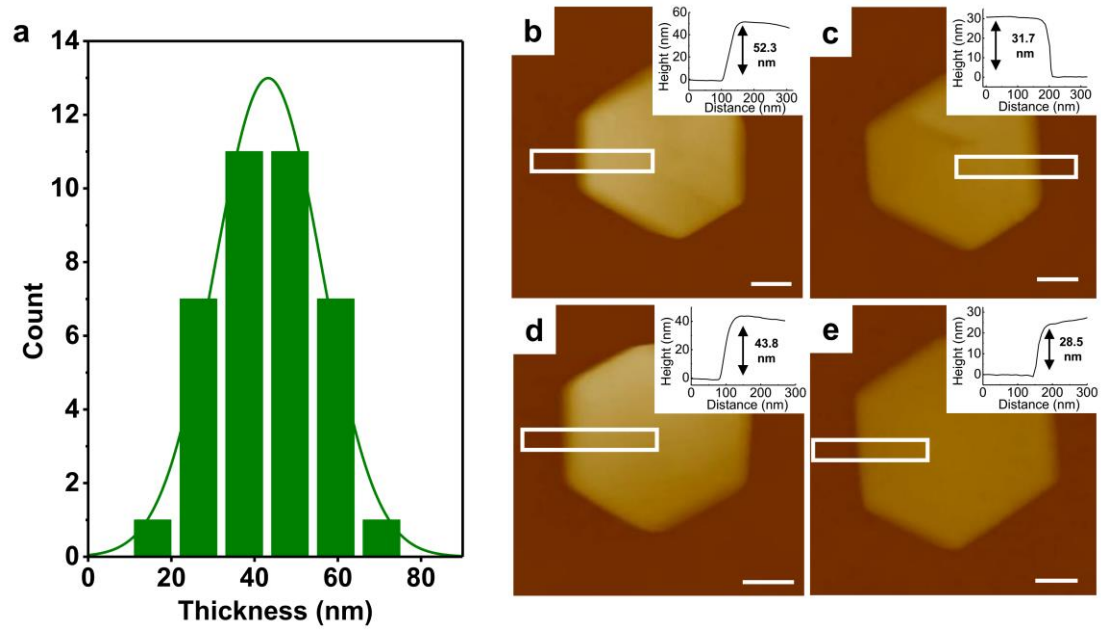

Supplementary Figure 2. (a) Thickness distribution of SnS_2 nanoplates showing a mean thickness of ~43 nm. (b-e) Examples of AFM images and height analyses of individual SnS_2 nanoplates (scale bars, 100 nm). Insets: height analysis of the region highlighted in the corresponding white rectangle.

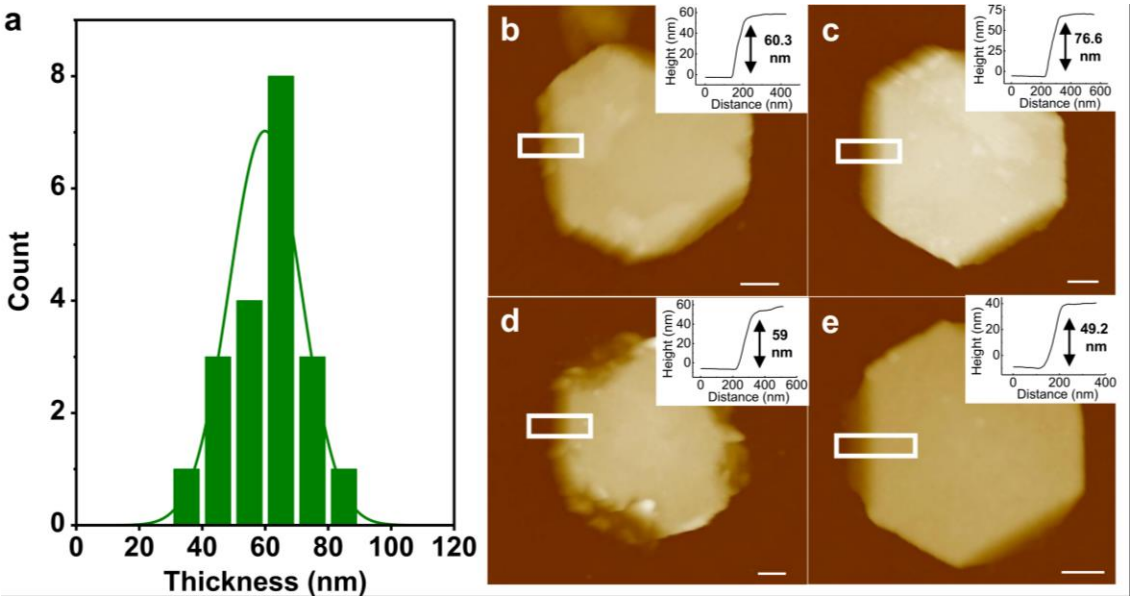

Supplementary Figure 3. (a) Thickness distribution of $Sn_{1-x}W_xS_2/SnS_2$ heterstructures, showing a mean thickness of ~60 nm. (b-e) Examples of AFM images and height analyses of individual $Sn_{1-x}W_xS_2/SnS_2$ heterstructures (scale bars, 100 nm). Insets: height analysis of the region highlighted in the corresponding white rectangle.

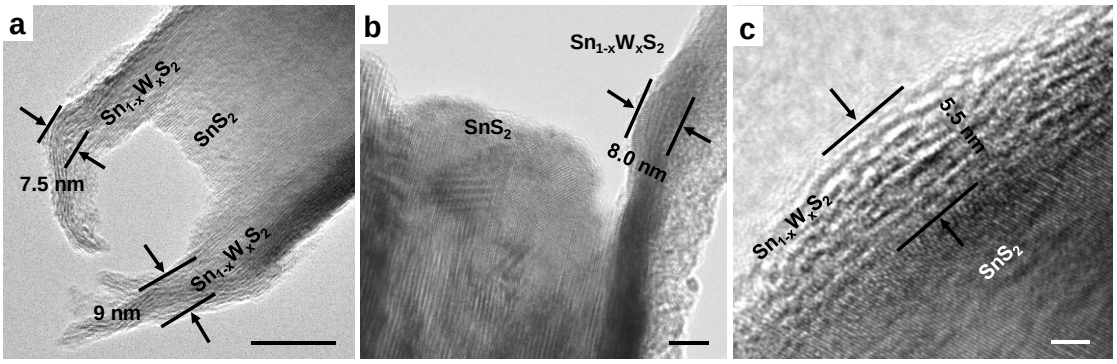

Supplementary Figure 4. (a-c) Side-view TEM images of typical $Sn_{1-x}W_xS_2/SnS_2$ heterostructures, revealing that the thickness of $Sn_{1-x}W_xS_2$ nanosheets grown on SnS_2 nanoplates is 6-9 nm. The scale bars in (a), (b) and (c) are 20 nm, 5 nm and 2 nm, respectively.

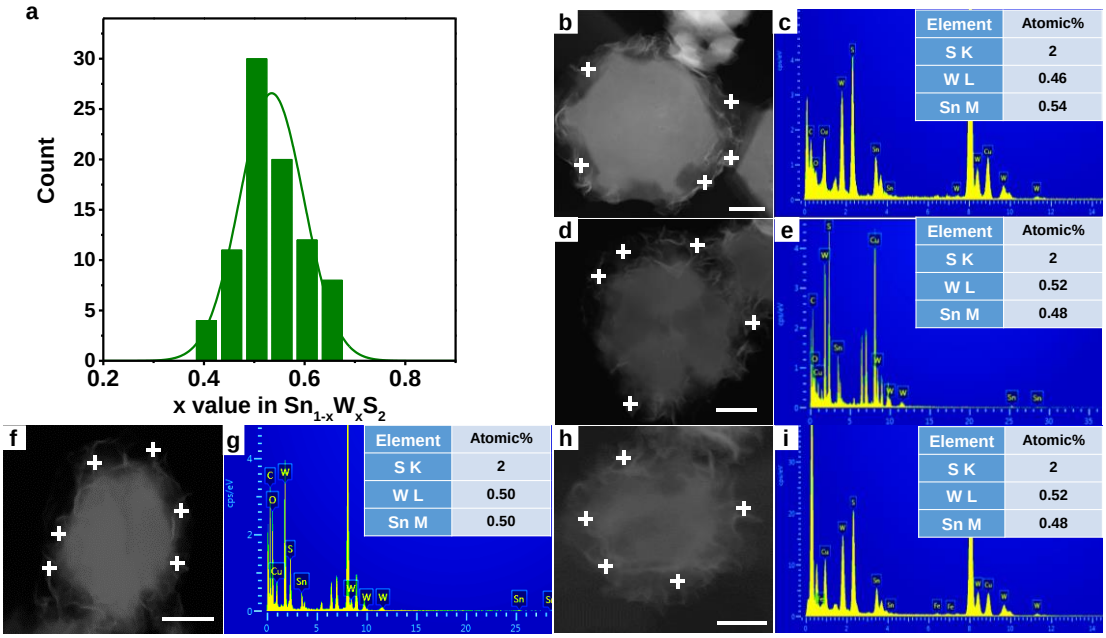

Supplementary Figure 5. (a) Distribution of x values in $Sn_{1-x}W_xS_2$ based on EDX spot analyses on the edges of several $Sn_{1-x}W_xS_2$. (b-i) Four examples of STEM images and EDX spot analyses on the edges of $Sn_{1-x}W_xS_2$ nanosheets, where the positions of the analyzed spots are highlighted in white crosses (scale bars, 200 nm). A mean value of ~0.5 was determined for x.

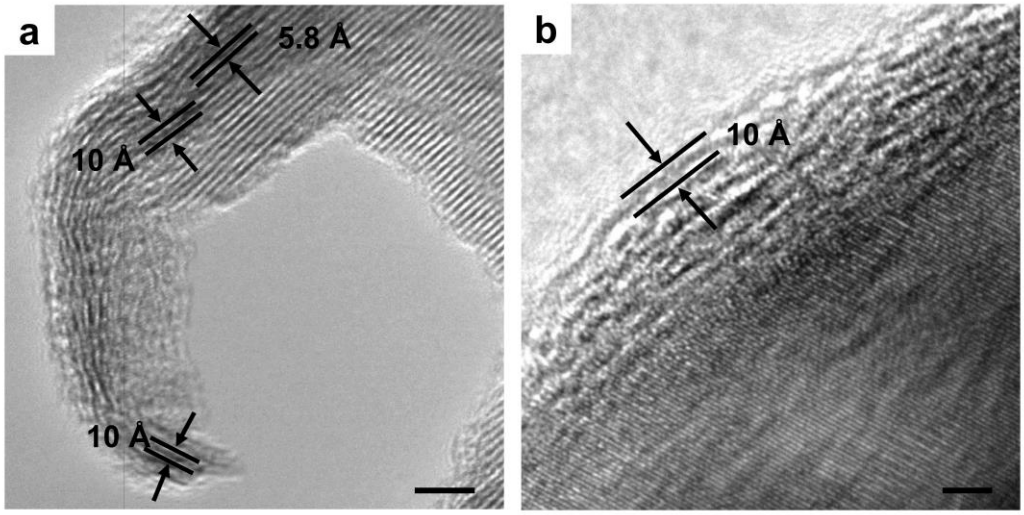

Supplementary Figure 6. (a,b) Side-view HRTEM images of typical $Sn_{0.5}W_{0.5}S_2/SnS_2$ heterostructures, revealing surface deposited $Sn_{0.5}W_{0.5}S_2$ nanosheets with varied interlayer spacings. The scale bars in (a) and (b) are 5 nm and 2 nm, respectively.

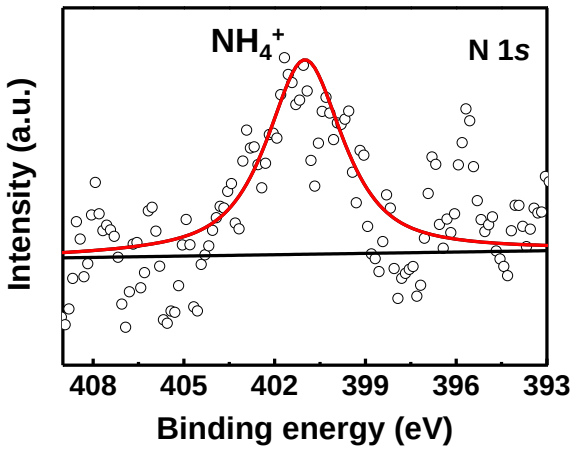

Supplementary Figure 7. XPS N 1*s* spectrum of as-prepared $Sn_{0.5}W_{0.5}S_2/SnS_2$ heterostructures, showing a peak at 401.1 eV, which can be assigned to NH_4^+ (ref. 2).

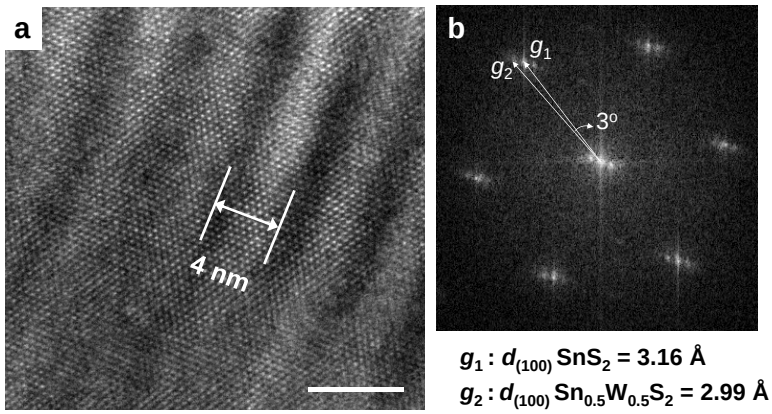

Supplementary Figure 8. (a) HRTEM image of a typical $Sn_{0.5}W_{0.5}S_2/SnS_2$ heterostructure lying flatly on a copper grid, showing a Moiré pattern with a periodicity of ~4.0 nm (scale bar, 5 nm). (b) Fast Fourier transform (FFT) diffraction pattern of (a), showing reciprocal vectors of g_1 and g_2 corresponding to the (100) planes of SnS_2 and $Sn_{0.5}W_{0.5}S_2$, with real space spacing d_1 and d_2 equaling to 3.16 and 2.99 Å, respectively. The Moiré pattern based on equation $d = \frac{d_1 d_2}{\sqrt{d_1^2 + d_2^2 - 2 d_1 d_2 \cos\theta}}$ has a calculated pattern periodicity of ~ 4.0 nm, consistent with the measurement in (a).

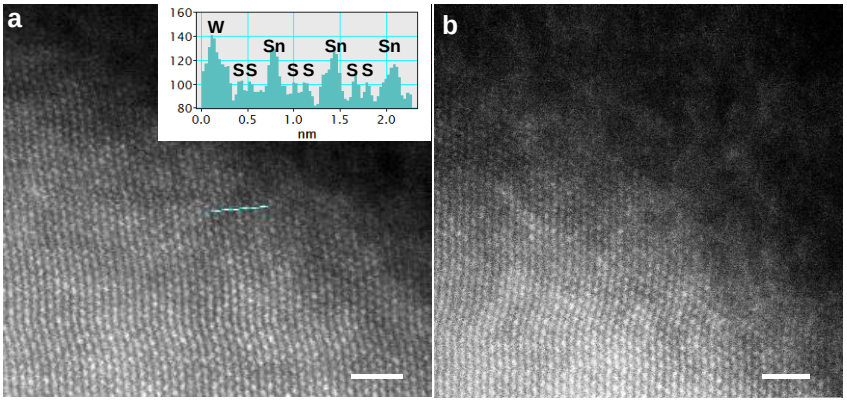

Supplementary Figure 9. (a,b) STEM images of the edge area of a typical $Sn_{0.5}W_{0.5}S_2/SnS_2$ heterostructure lying flatly on a copper grid (scale bars, 2 nm). The inset of (a) shows the contrast profile of the line marked in the image, indicating a typical metal-sulfur-sulfur-metal atomic pattern for 1T-phase-like structure[3]. From the thin area near the edge, contrast difference due to the presence of Sn and W elements can be observed.

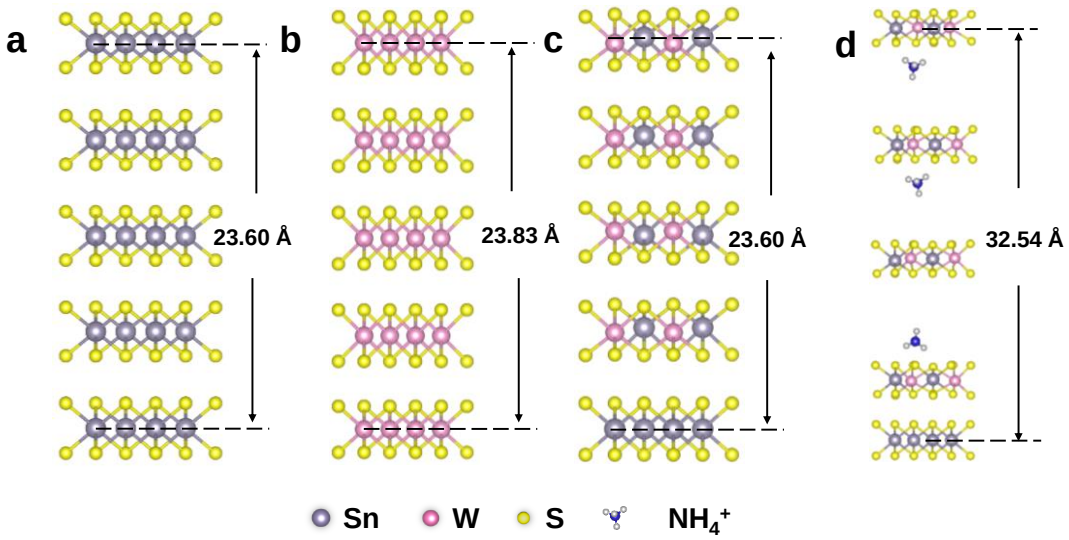

Supplementary Figure 10. Calculated structural models of (a) SnS_2, (b) 1T-WS_2, (c) a four-layer distorted 1T-$Sn_{0.5}W_{0.5}S_2$ on a monolayer 1T-SnS_2 and (d) a four-layer distorted 1T-$Sn_{0.5}W_{0.5}S_2$ on a monolayer 1T-SnS_2 with intercalated NH_4^+ ions. The optimized crystal structures of a five-layer SnS_2, a five-layer 1T-WS_2 and a four-layer distorted 1T-$Sn_{0.5}W_{0.5}S_2$ on a monolayer 1T-SnS_2 with and without NH_4^+ intercalated ions are shown in Fig. 10 and Table 1. In a 5-layer SnS_2, the Sn-S bond length is about 2.58 Å, while the W-S bond length in a 5-layer WS_2 is about 2.42 Å. The interlayer distance along the c-axis of SnS_2 is 5.90 ± 0.03 Å, shorter than that of WS_2 by ~0.10 Å. For $Sn_{0.5}W_{0.5}S_2$ without NH_4^+ intercalation, the bond lengths of Sn-S and W-S are 2.52 Å and 2.43 Å, respectively, and its interlayer distance along the c-axis is ~5.94 Å. Interestingly, after NH_4^+ intercalation, the bond length of Sn-S becomes longer (2.55 Å) and that of W-S becomes shorter (2.38 Å). The interlayer distance of $Sn_{0.5}W_{0.5}S_2$ with intercalated NH_4^+ ions also becomes larger.

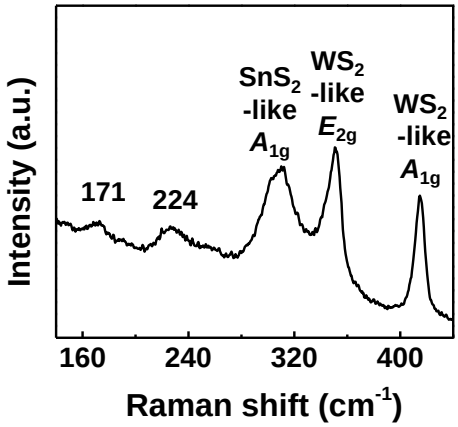

Supplementary Figure 11. Raman spectrum of as-prepared $Sn_{0.5}W_{0.5}S_2/SnS_2$ heterostructures.

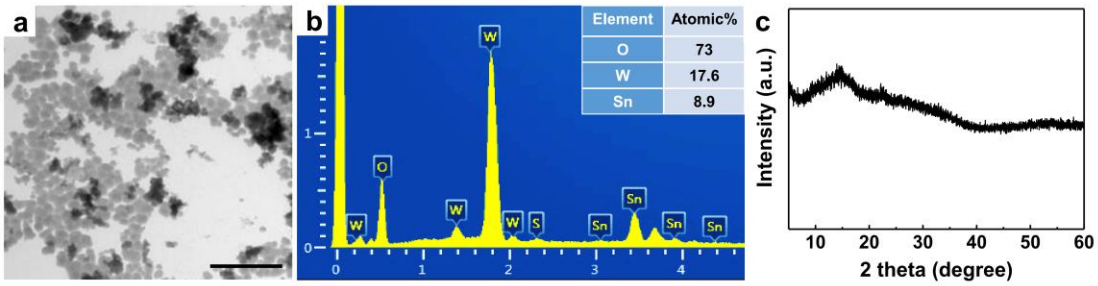

Supplementary Figure 12. (a) TEM image (scale bar, 500 nm), (b) EDX analysis and (c) XRD pattern of $Sn(HWO_4)_2 \cdot nH_2O$ nanoparticles formed during pre-treatment of precursors in an 80 °C water bath before hydrothermal reaction. The XRD pattern in (c) shows no obvious peaks, suggesting that the $Sn(HWO_4)_2 \cdot nH_2O$ nanoparticles were amorphous.

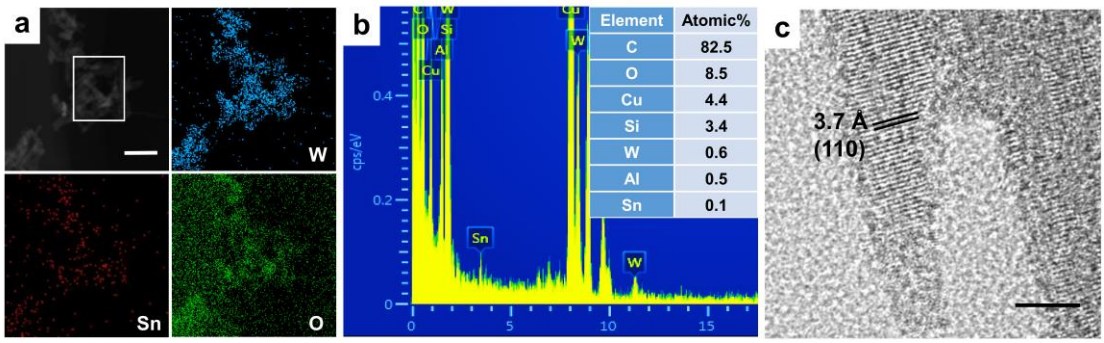

Supplementary Figure 13. (a) STEM image and EDS mapping of intermediate nanorods, confirming the presence of Sn and W elements (scale bar, 100 nm). (b) EDX analysis of the nanorods, where the position of the analyzed area is highlighted in the white rectangle in (a). The Sn:W ratio is about 0.1:0.6, suggesting that $Sn_{0.17}WO_3$ was obtained. (c) HRTEM image of the $Sn_{0.17}WO_3$ nanorods (scale bar, 5 nm). The measured lattice spacing of 3.7 Å can be assigned to the (110) planes of $Sn_{0.17}WO_3$ which show the same structure with previously reported $Sn_{0.23}WO_3$ (ICSD NO. 38043).

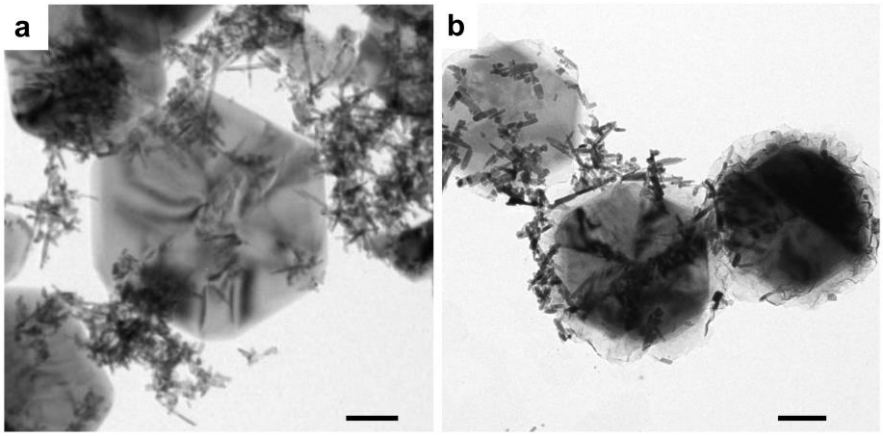

Supplementary Figure 14. TEM images of intermediate products obtained at reaction intervals of (a) 12 h and (b) 48 h, respectively. The scale bars, 200 nm.

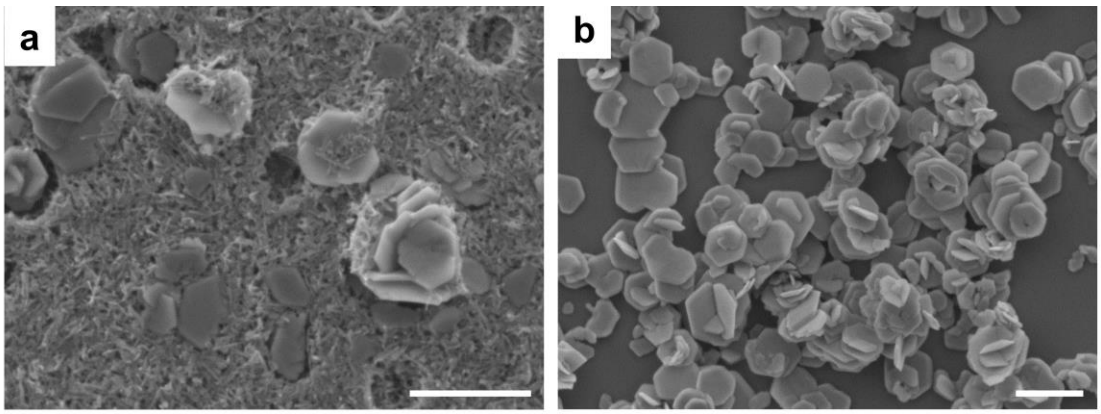

Supplementary Figure 15. SEM images of products synthesized at (a) 180 °C and (b) 200 °C for 60 h, respectively, without changing precursor concentrations (scale bars, 1 μm). It can be seen that $Sn_{0.17}WO_3$ nanorods could be prepared together with SnS_2 nanoplates at 180 °C, but were decomposed at 200 °C. $Sn_{0.5}W_{0.5}S_2$ nanosheets were not synthesized at 180 °C or 200 °C. This indicates that reaction at 220 °C with higher energy is needed for the synthesis of alloyed $Sn_{0.5}W_{0.5}S_2$. In addition, the quality of SnS_2 nanoplates prepared at 180 °C and 200 °C was not as good as those prepared at 220 °C.

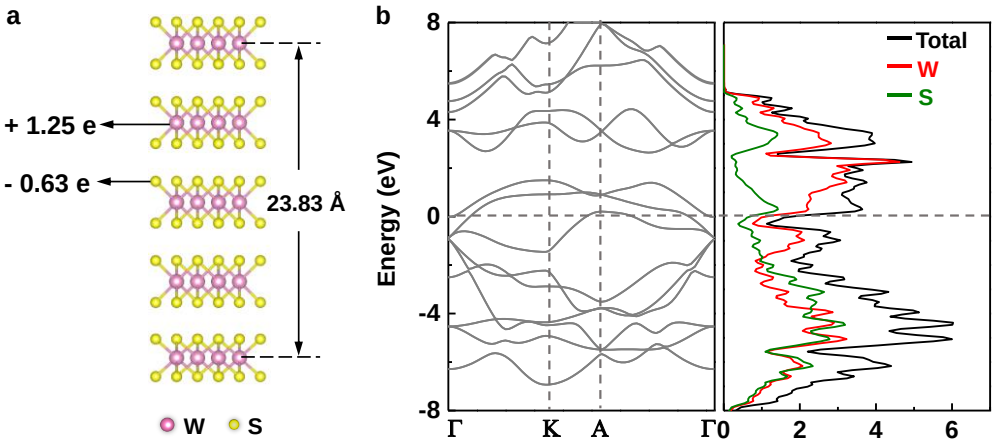

Supplementary Figure 16. (a) Optimized crystal structure with calculated Bader charges, (b) band structure and DOS of a 5-layer 1T-WS_2, demonstrating an intrinsic metallic behavior. The Fermi level is assigned at 0 eV.

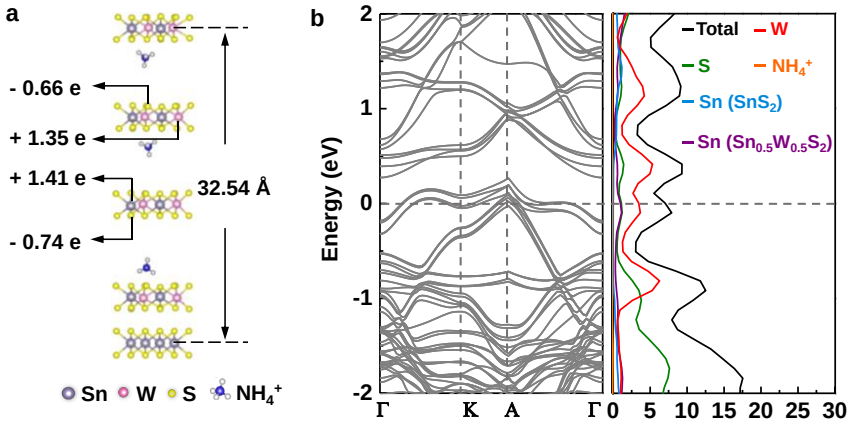

Supplementary Figure 17. (a) Optimized crystal structure with calculated Bader charges, (b) band structure and DOS of a four-layer distorted 1T-$Sn_{0.5}W_{0.5}S_2$ on a monolayer 1T-SnS_2 with intercalated NH_4^+ ions, showing an intrinsic metallic characteristic. The Fermi level is assigned at 0 eV.

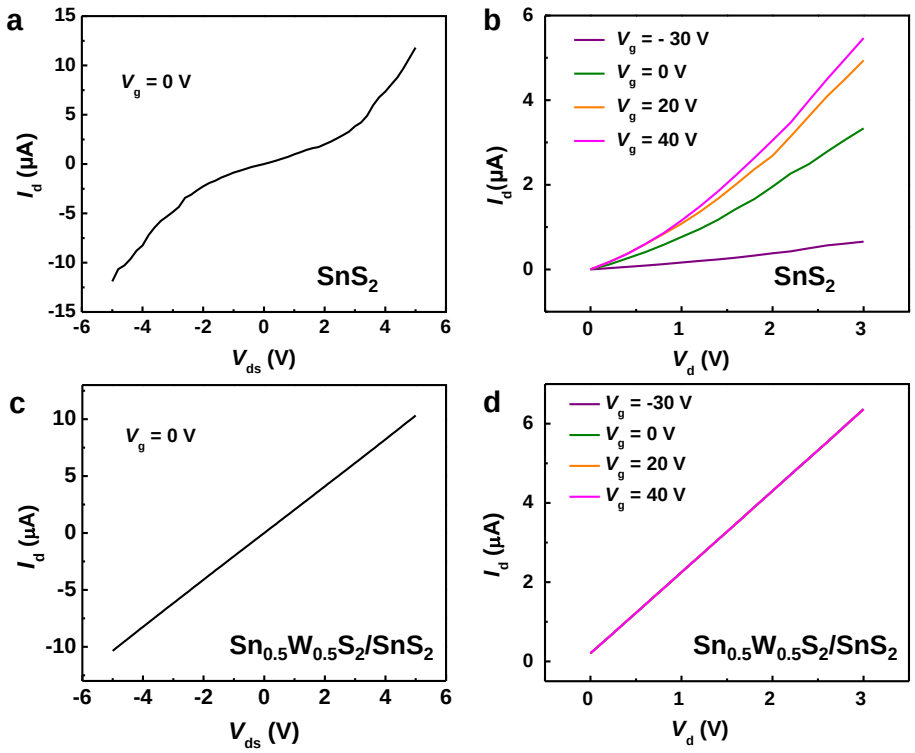

Supplementary Figure 18. Drain current (I_d) characteristics of back-gated TFTs based on (a) SnS_2 nanoplates and (c) $Sn_{0.5}W_{0.5}S_2/SnS_2$ heterostructures for drain-source voltages (V_{ds}) varied from -5 to 5 V at 0 V gate voltage (V_g). The I_d-V_{ds} curves of (b) SnS_2 nanoplates and (d) $Sn_{0.5}W_{0.5}S_2/SnS_2$ heterostructures at varied V_g from -30 to 40 V, measured in vacuum (5×10^{-5} Torr) at 77 K.

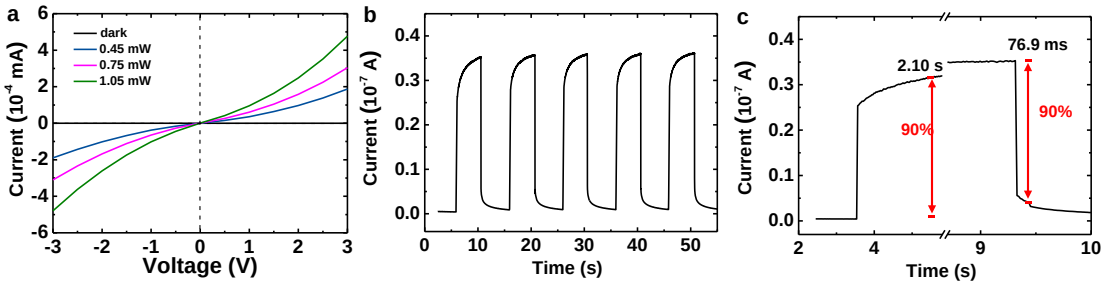

Supplementary Figure 19. (a) *I-V* curves at different light intensity, (b) temporal photocurrent response and (c) zoom-in view of the temporal photocurrent response of a thin film photodetector based on SnS_2 nanoplates.

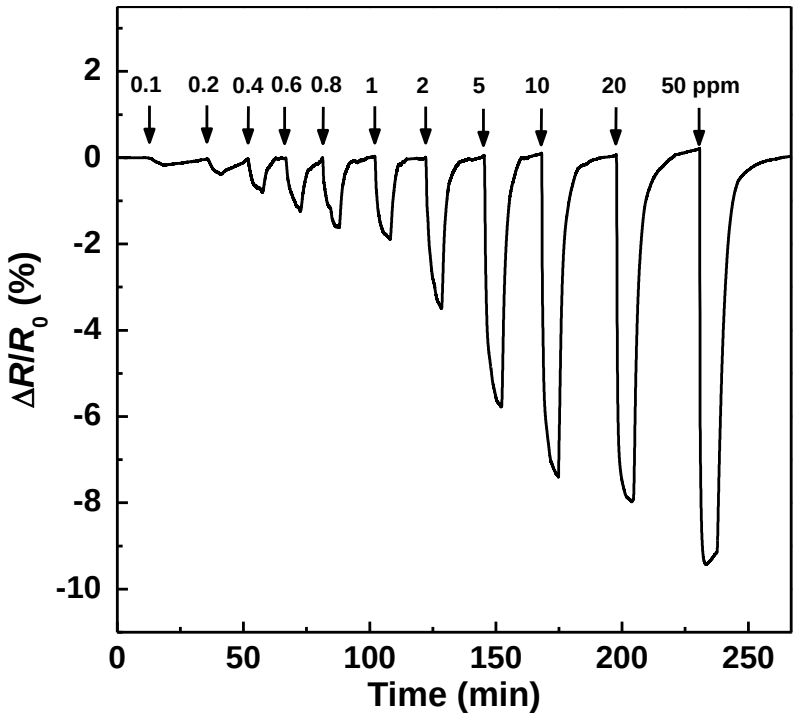

Supplementary Figure 20. Response-recover curve of a typical $Sn_{0.5}W_{0.5}S_2/SnS_2$-based sensor in response to acetone with different concentrations from 0.1 to 50 ppm.

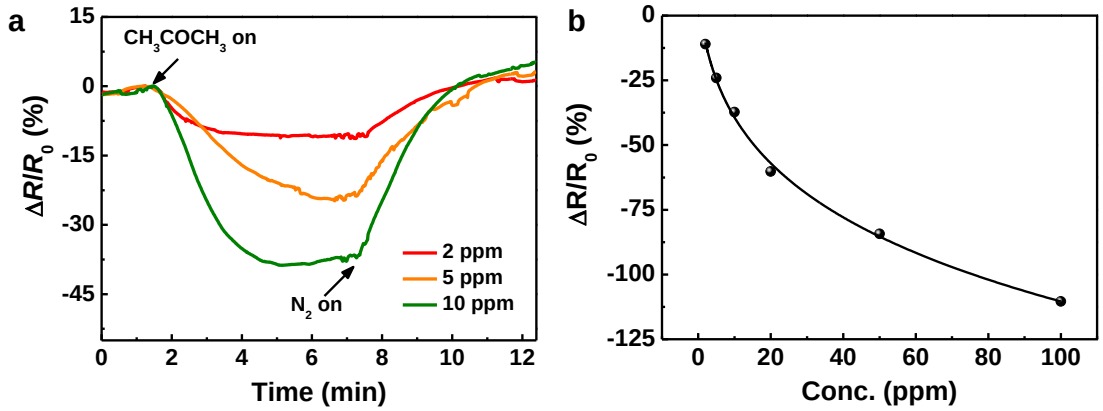

Supplementary Figure 21. (a) Response-recover curves of a typical SnS_2-based sensor in response to acetone with different concentrations from 2 to 10 ppm. (b) Normalized change of resistance of SnS_2 sensor at various acetone concentrations.

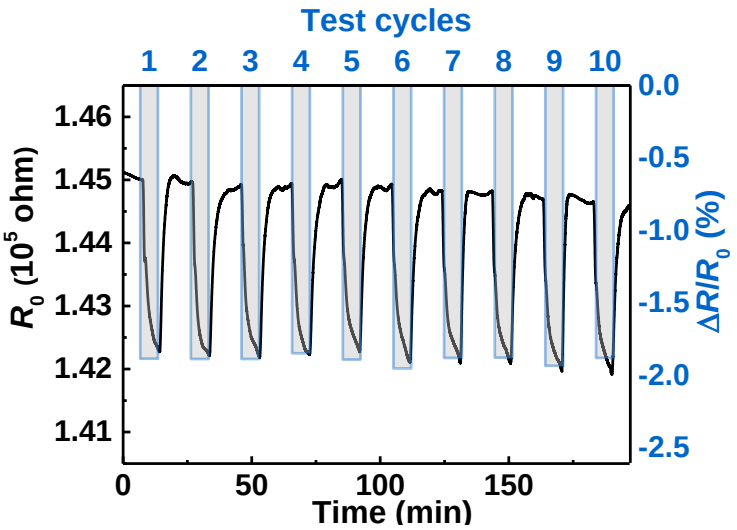

Supplementary Figure 22. Response-recover curve of $Sn_{0.5}W_{0.5}S_2/SnS_2$ heterostructure based sensor upon cyclic exposure to 1 ppm acetone. Overlayed bar chart: the corresponding responses for the tested 10 cylces.

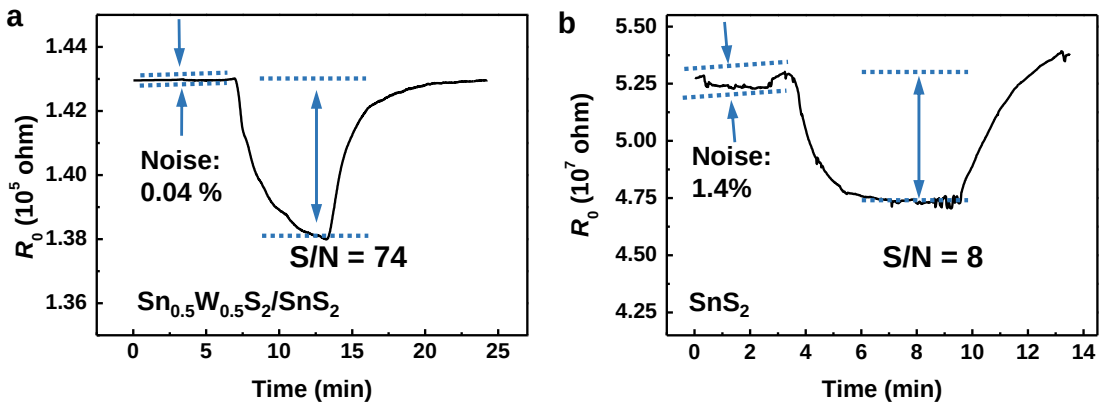

Supplementary Figure 23. The signal to noise ratios (S/N) of sensors based on (a) $Sn_{0.5}W_{0.5}S_2/SnS_2$ and (b) SnS_2 when responding to 2 ppm acetone.

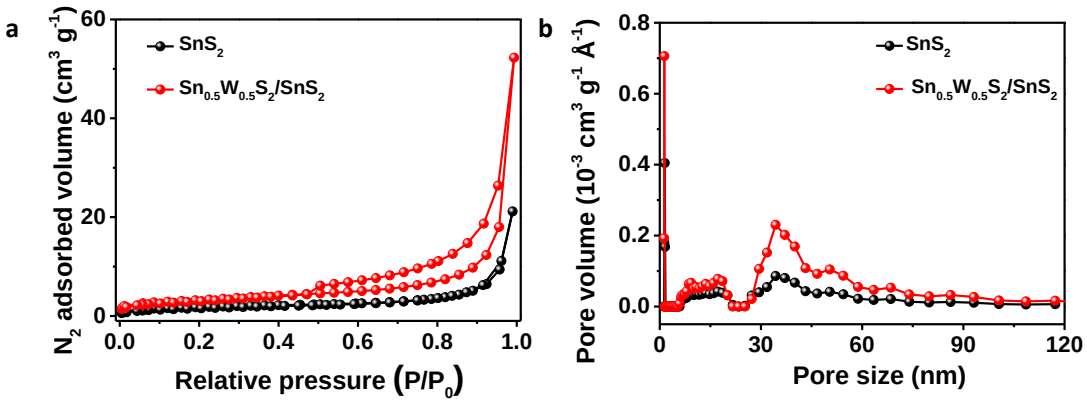

Supplementary Figure 24. (a) N_2 adsorption-desorption isotherms, and (b) DFT pore size distribution plots for SnS_2 nanoplates and $Sn_{0.5}W_{0.5}S_2/SnS_2$ heterostructures.

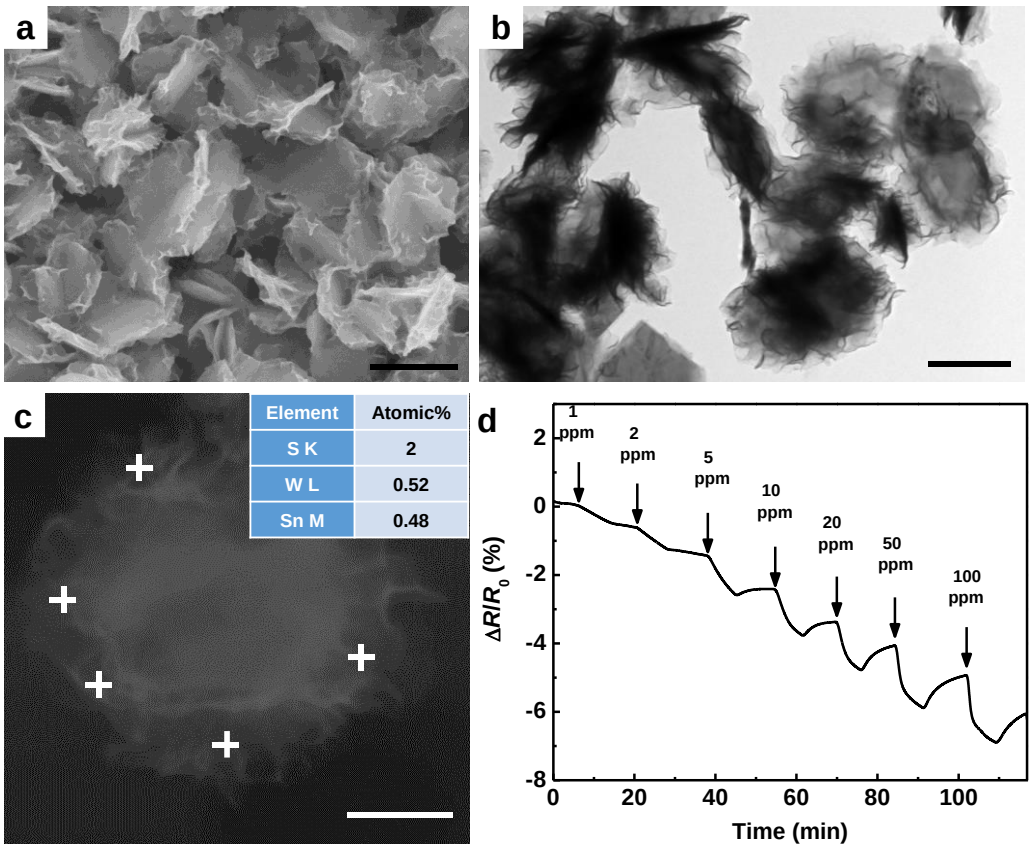

Supplementary Figure 25. (a) SEM image, (b) TEM image and (c) EDX spot analysis of $Sn_{0.5}W_{0.5}S_2/SnS_2$ heterostructures synthesized with precursors mixed at a Sn:W:S atomic ratio of 1:6:15. Increased amount of wrinkled $Sn_{0.5}W_{0.5}S_2$ nanosheets were found to encapsulate SnS_2 nanoplates. The scale bars in (a), (b) and (c) are 1 μm, 500 nm and 200 nm, respectively. (d) The response-recovery curve of the corresponding $Sn_{0.5}W_{0.5}S_2/SnS_2$ sensor upon exposure to acetone gas with increasing concentrations from 1 to 100 ppm.

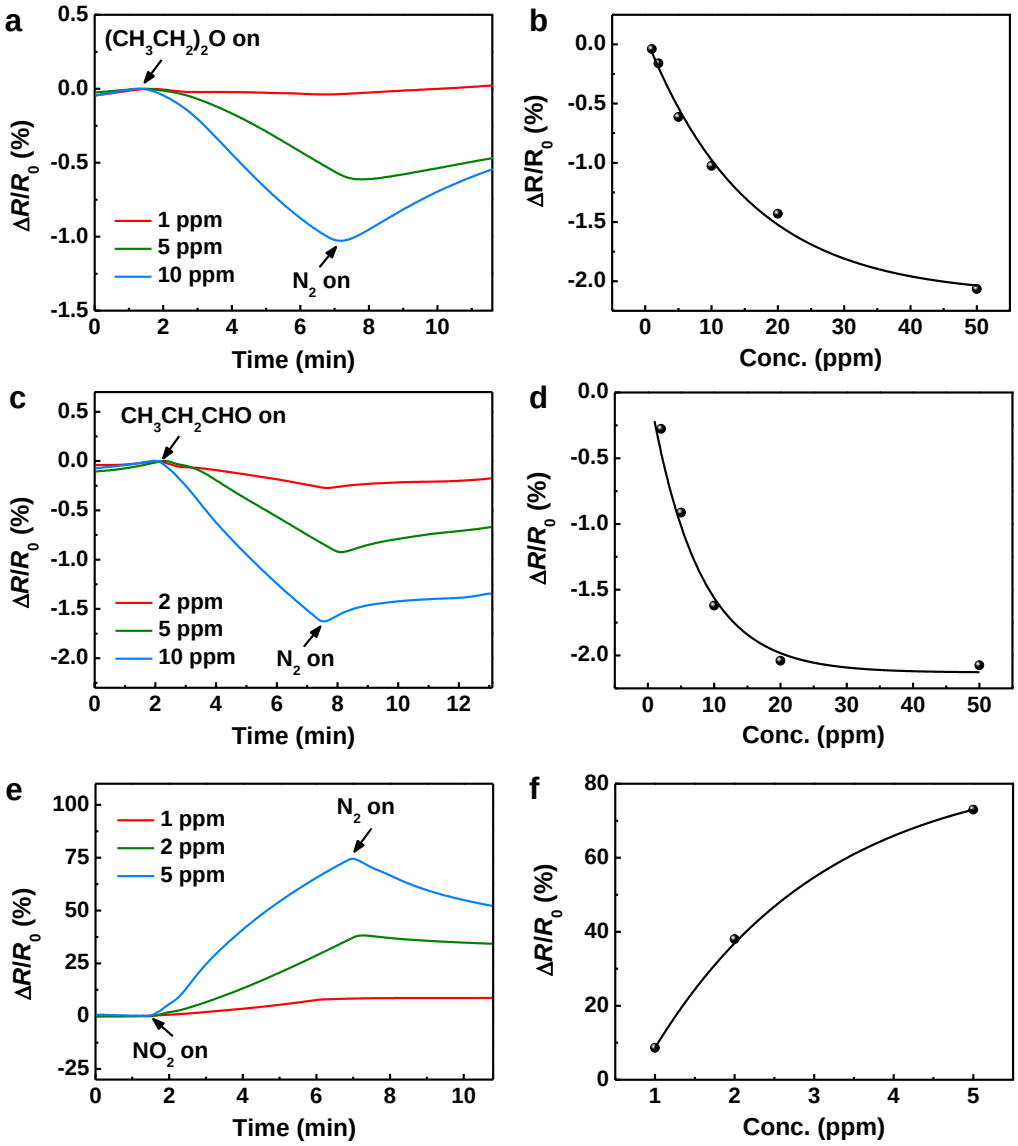

Supplementary Figure 26. Response-recover curves and normalized change of resistance of $Sn_{0.5}W_{0.5}S_2/SnS_2$ towards different gases including (a,b) diethyl ether, (c,d) propanal and (e,f) NO_2 at different concentrations.

Supplementary Tables

Supplementary Table 1. Optimized lattice parameters, bond lengths and work functions (Φ) of 1T-SnS_2, 1T-WS_2 and a four-layer $Sn_{0.5}W_{0.5}S_2$ on a monolayer 1T-SnS_2 without and with intercalated NH_4^+ ions.

System	*a* (Å)	*b* (Å)	*c* (Å)	*α* (°)	*β* (°)	*γ* (°)	Sn-S bond length (Å)	W-S bond length (Å)	*Φ* (eV)
SnS_2	3.65	3.65	23.60	90	90	120	2.58	-	5.27
WS_2	3.15	3.15	23.83	90	90	120	-	2.42	6.62
$Sn_{0.5}W_{0.5}S_2$	3.46*	3.46*	23.34	90	90	120	2.52	2.43	5.62
NH_4^+-intercalated $Sn_{0.5}W_{0.5}S_2$	3.46*	3.46*	32.54	90	90	120	2.55	2.38	2.81

* The experimental lattice constant (3.46 Å) was used in our calculations for the in-plane periodicity of the four-layer $Sn_{0.5}W_{0.5}S_2$ on a monolayer 1T-SnS_2 without and with NH_4^+-intercalated systems.

Supplementary Table 2. Concentrations of Sn and W ions measured by ICP-MS for solutions obtained at different reaction intervals.

Ions	5 h	12 h	24 h	48 h	60 h
Sn (μmol/L)	47.2	26.1	31.2	37.1	18.5
W (μmol/L)	566.2	877.9	1482.3	1283.2	1013.9

Supplementary Table 3. Comparison between our $Sn_{0.5}W_{0.5}S_2/SnS_2$-based sensor and other reported chemiresistive acetone gas sensors operating at room temperature.

Materials	Temperature (°C)	Sensor type	Minimum detectable concentration (ppm)	Response at 0.4 ppm (%)	Response at 0.2 ppm (%)	Ref.
$Sn_{0.5}W_{0.5}S_2/SnS_2$	25	Chemiresistor	0.1	0.60	0.37	This work
SnS_2	25	Chemiresistor	2.0	n.d.	n.d.	This work
MoS_2	25	Chemiresistor	1.0	n.d.	n.d.	4
SnS	25	Chemiresistor	10	n.d.	n.d.	5
Co_3O_4-ZnS	25	Chemiresistor	10	n.d.	n.d.	6
$Ti_3C_2T_x$	25	Chemiresistor	0.05	0.25*	0.18*	7
V_2O_5	25	Chemiresistor	0.9	n.d.	n.d.	8
WO_3-polyaniline	25	Chemiresistor	10	n.d.	n.d.	9
TiO_2	27	Chemiresistor	10	n.d.	n.d.	10
Pt-SnO_2	25	Chemiresistor	10	n.d.	n.d.	11
SnO_2-RGO	25	Chemiresistor	10	n.d.	n.d.	12
ZnO	25	Chemiresistor	2.0	n.d.	n.d.	13
C-ZrO_2	25	Chemiresistor	10	n.d.	n.d.	14
Ce-ZnO	24	Chemiresistor	1.0	n.d.	n.d.	15
InGa-ZnO	25	Chemiresistor	50	n.d.	n.d.	16
$La_{1-x}Sr_xCoO_3$	25	Chemiresistor	10	n.d.	n.d.	17
VO_2	25	Chemiresistor	5.0	n.d.	n.d.	18
$ZnWO_4$	23	Chemiresistor	100	n.d.	n.d.	19
TsCuPc/ZnO	35	Chemiresistor	50	n.d.	n.d.	20
Carbon onions	25	Chemiresistor	37	n.d.	n.d.	21

n.d. means non-detectable.

* denotes estimated value from the reported normalized response curve.

Supplementary References

1 Ou, J. Z. *et al.* Physisorption-based charge transfer in two-dimensional SnS_2 for selective and reversible NO_2 gas sensing. *ACS Nano* **9**, 10313-10323 (2015).

2 Liu, Q. *et al.* Gram-scale aqueous synthesis of stable few-layered 1T-MoS_2: applications for visible-light-driven photocatalytic hydrogen evolution. *Small* **11**, 5556-5564 (2015).

3 Eda, G. *et al.* Coherent atomic and electronic heterostructures of single-layer MoS_2. *ACS Nano* **6**, 7311-7317 (2012).

4 Kim, J. S., Yoo, H. W., Choi, H. O. & Jung, H. T. Tunable volatile organic compounds sensor by using thiolated ligand conjugation on MoS_2. *Nano Lett.* **14**, 5941-5947 (2014).

5 Afsar, M. F., Rafiq, M. A. & Tok, A. I. Y. Two-dimensional SnS nanoflakes: synthesis and application to acetone and alcohol sensors. *RSC Adv.* **7**, 21556-21566 (2017).

6 Park, S., Sun, G.-J., Kim, S., Lee, S. & Lee, C. UV-enhanced acetone gas sensing of Co_3O_4-decorated ZnS nanorod gas sensors. *Electron. Mater. Lett.* **11**, 572-579 (2015).

7 Kim, S. J. *et al.* Metallic $Ti_3C_2T_x$ MXene gas sensors with ultrahigh signal-to-noise ratio. *ACS Nano* **12**, 986-993 (2018).

8 Hakim, S. A., Liu, Y. L., Zakharova, G. S. & Chen, W. Synthesis of vanadium pentoxide nanoneedles by physical vapour deposition and their highly sensitive behavior towards acetone at room temperature. *RSC Adv.* **5**, 23489-23497 (2015).

9 Hicks, S. M. & Killard, A. J. Electrochemical impedance characterisation of tungsten trioxide–polyaniline nanocomposites for room temperature acetone sensing. *Sensors and Actuators B* **194**, 283-289 (2014).

10 Bhowmik, B., Hazra, A., Dutta, K. & Bhattacharyya, P. Repeatability and stability of room-temperature acetone sensor based on TiO_2 nanotubes: influence of stoichiometry variation. *IEEE Trans. Device Mater. Rel.* **14**, 961-967 (2014).

11 Shao, S. *et al.* Highly crystalline and ordered nanoporous SnO_2 thin films with enhanced acetone sensing property at room temperature. *J. Mater. Chem. C* **3**, 10819-10829 (2015).

12 Zhang, D., Liu, A., Chang, H. & Xia, B. Room-temperature high-performance acetone gas sensor based on hydrothermal synthesized SnO_2-reduced graphene oxide hybrid composite. *RSC Adv.* **5**, 3016-3022 (2015).

13 Muthukrishnan, K. *et al.* Studies on acetone sensing characteristics of ZnO thin film prepared by sol–gel dip coating. *J. Alloys. Compd.* **673**, 138-143 (2016).

14 Dankeaw, A., Poungchan, G., Panapoy, M. & Ksapabutr, B. In-situ one-step method for fabricating three-dimensional grass-like carbon-doped ZrO_2 films for room temperature alcohol and acetone sensors. *Sensors and Actuators B* **242**, 202-214 (2017).

15 Kulandaisamy, A. J. *et al.* Nanostructured Cerium-doped ZnO thin film – A breath sensor. *Ceram. Int.* **42**, 18289-18295 (2016).

16 Jaisutti, R., Kim, J., Park, S. K. & Kim, Y. H. Low-temperature photochemically activated amorphous indium-gallium-zinc oxide for highly stable room-temperature gas sensors. *ACS Appl. Mater. Interfaces* **8**, 20192-20199 (2016).

17 Liu, H. *et al.* Novel acetone sensing performance of $La_{1-x}Sr_xCoO_3$ nanoparticles at room temperature. *Sensors and Actuators B* **246**, 164-168 (2017).

18 Simo, A., Kaviyarasu, K., Mwakikunga, B., Mokwena, M. & Maaza, M. Room temperature volatile organic compound gas sensor based on vanadium oxide 1-dimension nanoparticles. *Ceram. Int.* **43**, 1347-1353 (2017).

19 Li, C. *et al.* Enhancement of gas-sensing abilities in p-type $ZnWO_4$ by local modification of Pt nanoparticles. *Anal. Chim. Acta* **927**, 107-116 (2016).

20 Bal, A. K. Room-temperature acetone sensing by sulfonated copper phthalocyanine (TsCuPc)-modified ZnO films. *J. Electron. Mater.* **44**, 144-151 (2014).

21 Dhonge, B. P., Motaung, D. E., Liu, C.-P., Li, Y.-C. & Mwakikunga, B. W. Nano-scale carbon onions produced by laser photolysis of toluene for detection of optical, humidity, acetone, methanol and ethanol stimuli. *Sensors and Actuators B* **215**, 30-38 (2015).